

Determination of indium melting curve at high pressure by picosecond acoustics

Simon Ayrinhac ^{*}, Michel Gauthier , Marc Morand , Yuri Garino , Silvia Boccato , Frédéric Decremps , Paraskevas Parisiades , Philippe Rosier [†], Nicki C. Siersch , Abderraouf Seghour , and Daniele Antonangeli 

Sorbonne Université, Muséum National d'Histoire Naturelle, UMR CNRS 7590,

Institut de Minéralogie, de Physique, des Matériaux, et de Cosmochimie, IMPMC, 75005 Paris, France



(Received 16 February 2022; accepted 20 April 2022; published 16 June 2022)

Picosecond acoustics combined with a diamond anvil cell is used to study liquid indium and to determine with high accuracy both the sound velocity and the melting curve over an extended pressure and temperature range. The sound velocities, determined by phonon surface imaging, complement previous inelastic x-ray scattering determinations and are in good agreement with estimations according to a thermodynamic model. Based on exact thermodynamic relations, the equation of state of the liquid phase is obtained using the isothermal bulk modulus $B_{T,0}$ and its first pressure derivative B'_T . These quantities are derived from the precise experimental determination of the variation of the sound velocity as a function of pressure. Melting is determined via the detection of abrupt changes in the elastic properties between solid and liquid phases and through the monitoring of the solid-liquid coexistence. The melting curve constrained up to 6 GPa and 673 K is shown to be well described by the Simon-Glatzel equation in the full (p, T) range explored.

DOI: [10.1103/PhysRevMaterials.6.063403](https://doi.org/10.1103/PhysRevMaterials.6.063403)

I. INTRODUCTION

Determination of the thermoelastic properties of liquids at extreme conditions of pressure and temperature is fundamental for understanding the properties of condensed matter (e.g., [1,2]), with direct implications in geophysics and planetary sciences (e.g., [3–6]). Even though it is an experimentally challenging task, many previous studies dealt with the determination of phase diagrams, including melting curves, equations of state, or sound velocity measurements in the liquid phase, in addition to the determination of other thermodynamic properties such as bulk modulus or thermal expansion. In particular, many techniques were developed to measure the melting curves (see [7,8] for a review). Early methods were based on visual observations [9,10], the existence of a temperature plateau [11], or changes in electrical resistivity [12]. More recent *in situ* diagnostics include the appearance of diffuse signal in x-ray diffraction [13,14], characteristic changes in the x-ray absorption spectroscopy [15], and detection by synchrotron Mössbauer spectroscopy experiments [16].

During the last decades, picosecond acoustics (PA) combined with a diamond anvil cell (DAC) has been increasingly used to measure the thermoelastic properties of liquids and solids as well as their phase diagram. Nowadays, the combination of these two techniques appears to be a powerful and versatile laboratory tool [17] used to accurately measure both the melting curve and the sound velocities under high temperature and pressure conditions [18–20]. So far, PA has

been successfully applied to study various solids (e.g., ice [21,22], Ar [23], H [24]) and liquids (e.g., Hg [25,26], Ga [18], Rb [20], Cs [19]).

To further explore the detection and metrology capabilities of PA, liquid indium can be considered a very interesting case study. First of all, its properties are very well known at ambient pressure [27,28], making indium a standard calibration substance [29,30]. In particular, its melting temperature is a secondary reference point of the international temperature scale (ITS) [31]. Second, due to its low melting temperature, ductility, and low chemical reactivity [32], indium can be routinely handled in the laboratory. Third, although there are many papers on the measurements of sound velocities in liquid indium at high temperatures and ambient pressure (see for example the review of Blairs [33]), experimental data at gigapascal pressures are very scarce. To the best of our knowledge, the sound velocities at high pressure were measured only by Coppens *et al.* [34] up to around 0.01 GPa, and by Alatas *et al.* [35] and Komabayashi *et al.* [36] up to 6.7 GPa. Finally, the phase diagram of solid indium appears to be unusual compared to other III-A group elements (Al, Ga, Tl) and has attracted interest over time [37–41]. At ambient conditions, indium crystallizes in a tetragonal distortion of the face-centered cubic (FCC) system. This face-centered tetragonal structure (FCT) is stable at ambient temperature up to 50 GPa [41]. The c/a ratio is observed to reach a maximum value around 20 GPa [37,41], which is related to an increased distortion of the FCT structure with respect to FCC. Above 50 GPa a solid-solid transition occurs and the indium structure changes from FCT to a face-centered orthorhombic (FCO) arrangement, stable up to ≈ 150 GPa [41]. The indium phase diagram was also explored by *ab initio* electronic structure calculations at $T = 0$ K [42], and at high temperatures by XRD ($T > 500$ K) [43], but no other transitions were reported in the solid phase up to 247 GPa [41]. From all the above, we

^{*}simon.ayrinhac@sorbonne-universite.fr

[†]Present address: Université Paris-Saclay, CNRS UMR 9012, Laboratoire de Physique des 2 Infinis Irène Joliot-Curie (IJCLab), 91405 Orsay, France.

can conclude that indium is particularly stable at high pressure and temperature compared to other metallic elements [44].

Regarding the liquid phase, although the melting point is well known at ambient pressure, the melting curve measured by several authors with different techniques shows significant discrepancies above 4 GPa [45]. The knowledge of the melting curve is actually crucial as it is used as a calibration curve at high p and high T (see, for example, Ref. [36]). This calls for a new set of experimental data obtained using a state of the art technique, with particular attention dedicated to both the detection criteria of the solid-liquid transition, and the accurate pressure and temperature metrology.

Sound velocities in solids and liquids are markedly different and changes in sound velocities are a very sensitive probe to detect a solid-liquid phase transition [18,46,47] or subtle transformations in the liquid phase [19,20]. Furthermore, accurate velocity measurements allow us to derive useful thermodynamical quantities and to obtain the equation of state of the liquid [48,49]. We have thus reexamined the properties of liquid indium in the temperature range 420–680 K and from ambient pressure to 6 GPa by the PA technique combined with an externally heated diamond anvil cell (hDAC).

II. EXPERIMENTAL METHODS AND SETUP

A. Picosecond acoustics setup

Picosecond acoustics is a time-resolved, pump-probe, optical technique that generates and detects propagating strain waves in solids or liquids [50,51].

In our setup, the infrared beam from a mode-locked Ti:sapphire laser [$\lambda = 960$ nm, pulse width 100 fs, repetition rate ≈ 80 MHz, i.e., $T_{\text{laser}} = 12.548(4)$ ns] is divided into a pump and a probe beam (see Fig. 1).

The pump beam passes through an acousto-optic modulator (AOM), which modulates the intensity of the pump beam around 1 MHz, to improve the signal-to-noise ratio through lock-in detection (HF2LI from Zurich Instruments). Then the pump beam is focused onto one of the surfaces of the sample (beam waist ≈ 1.5 μm), and, for metallic samples as the case of present interest, directly absorbed. The so-generated thermal stress relaxes and an acoustic wave propagates into the sample.

The probe beam is delayed with respect to the pump by a mechanical delay line (optical length 4 m, maximum delay time 13.33 ns) and focused on the opposite surface of the sample to detect its reflectivity changes due to the arrival of the acoustic wave.

These changes in reflectivity can be detected on the variation either in the intensity or in the phase of the reflectivity signal. The intensity variation $\rho = \text{Re}(\Delta R/R)$ is related to the photoelastic properties of the sample. Unfortunately, the photoelastic variation induced in indium is very small and a reflectivity measurement setup is not efficient enough in this case. An interferometric system should be used instead.

By means of a beam splitter, the probe beam is divided into two. One part is focused on the sample with the use of an objective mounted on an XY piezoelectric stage (P-517.2CL from Physik Instrumente) exploited to scan the sample surface over a 100×100 μm^2 area and collect surface phonon

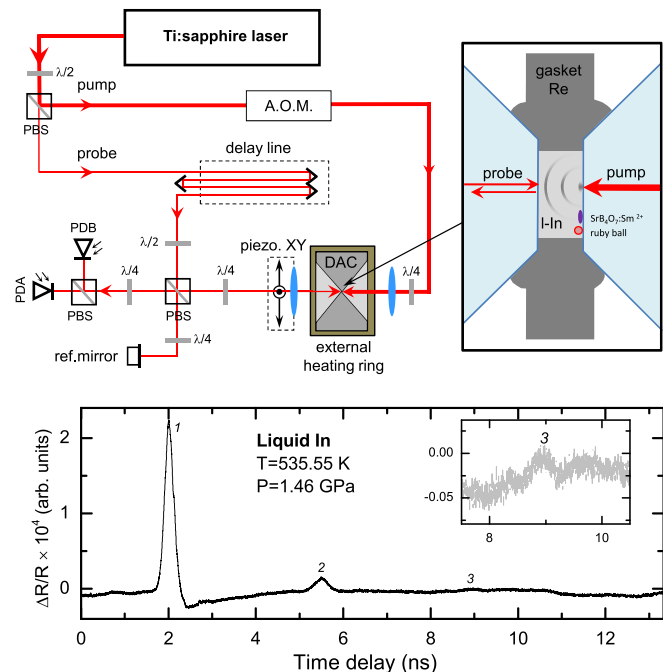


FIG. 1. Top: Schematic view of the setup. PBS: Polarizing beam splitter, $\lambda/2$: Half-wave plate, $\lambda/4$: Quarter-wave plate, PD: Amplified photodetector, “A.O.M.” stands for acousto-optic modulator, and “ref. mirror” for reference mirror as a part of a Michelson interferometer. Blue ellipses represent optical objectives. Bottom: Interferometric signal as a function of delay time obtained in liquid indium at high pressure and temperature with collinear pump and probe beams. Numbers identify consecutive echoes corresponding to the n th wave arriving at the sample surface on the probe side. Inset: Magnification of the third echo.

imaging data [52]. The remaining part of the probe beam is reflected on a reference mirror mounted on a piezoactuator with a feedback loop to stabilize the Michelson interferometer [53,54]. The two beams reflected by the sample and the reference mirror are then mixed to obtain interferences before being collected by two amplified photodetectors. The voltage difference $V_A - V_B$ between the two photodetectors (PDA and PDB in Fig. 1) is proportional to the phase change of the relative reflectivity variation $\phi = \text{Im}(\Delta R/R)$. The obtained signal shown in Fig. 1 (bottom) is thus affected by both the sample surface displacement and its refractive index variations through the photoelastic effect [51].

B. Metrology: Determination of pressure and temperature

Measurements are performed in a restively heated diamond anvil cell, equipped with a pair of diamonds with culets of 600 μm and a pre-indented rhenium gasket. The large culets are chosen to facilitate surface phonon imaging as a sample with a diameter larger than 100 μm and a thickness of tens of microns is needed. Heating is achieved by an external resistive heater, whose power is controlled by the target temperature measured by a K-type thermocouple located between the DAC and the resistive heater, and tuned by a PID controller. A second thermocouple is glued in contact with one of the diamonds.

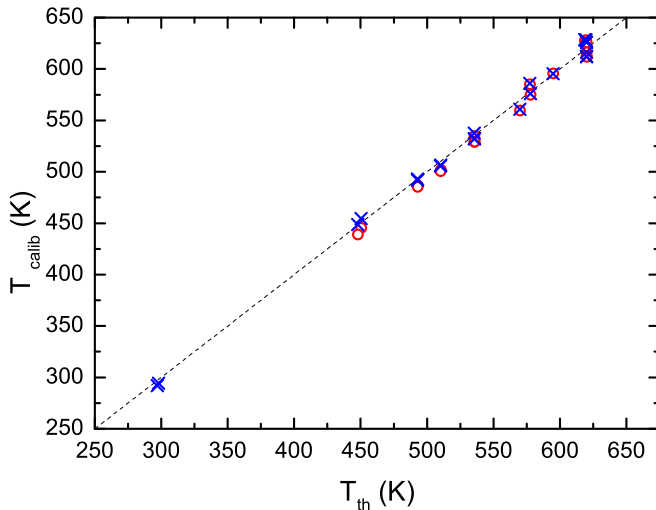


FIG. 2. Temperature estimated from the *in situ* optical sensors T_{calib} (see text and [58], Sec. I) as a function of the temperature value T_{th} provided by the thermocouple glued to one of the diamonds of the DAC. The analysis of the ruby fluorescence line shift is performed according to two models, Datchi *et al.* [55] (red empty circles) and McCumber *et al.* [59] (blue crosses). The equality relation is indicated by the dashed line.

The indium sample (127 μm thick foil from Sigma-Aldrich Chemie GmbH, purity 99.99% metal basis) is loaded at ambient conditions in a hole drilled in the rhenium gasket with a diameter of 340 μm and a thickness around 50 μm (a scheme of the sample chamber can be visualized in Fig. 1). The indium sample entirely fills the hole and plays both the role of metallic transducer and pressure-transmitting medium when in the liquid state. Even when solid, being a soft metal, it does not sustain strong uniaxial stress and this deviatoric stress vanishes each time the sample melts.

A Sm-doped strontium tetraborate ($\text{SrB}_4\text{O}_7:\text{Sm}^{2+}$) optical sensor is used as an *in situ* pressure gauge [55], as the shift of the ${}^7D_0\text{-}{}^5F_0$ fluorescence line depends on the applied pressure but is almost independent of temperature. In addition, a ruby sphere (3000 ppm Cr-doped corundum: $\text{Al}_2\text{O}_3:\text{Cr}^{3+}$) [56] is placed inside the sample chamber and, in this case, the shift of the luminescence signal is sensitive to both p and T [57].

The fluorescence signal of the two calibrants is excited by a CW sapphire laser from Coherent, Inc., operating at $\lambda = 488$ nm.

The combined use of the two *in situ* sensors allows us not only to probe pressure, but as well to perform an independent check of the T values measured by the thermocouple. In practice, being almost insensitive to T , the shift in the signal of the Sm-doped strontium tetraborate directly provides the pressure. The temperature can then be determined by the ruby calibrant by imposing in the signal analysis the pressure determined from the Sm-doped strontium tetraborate (see [58], Sec. I).

As shown in Fig. 2, there is an excellent agreement between the temperature provided by the thermocouple glued to the diamond and the temperature estimated from the *in situ* sensors according the two models. Unfortunately the ruby sphere disappeared inside the liquid before performing

measurements at the highest isotherm (680 K). However, since the value of temperature given by the thermocouple was proven reliable for all other temperatures, this has been used for all the p - T measurements.

The uncertainty on temperature measurements from the thermocouple is evaluated to be ± 2 K and on pressure measurements determined from the Sm-doped strontium tetraborate calibrant to be 0.1–0.2 GPa.

III. EXPERIMENTAL RESULTS

A. Sound velocity measurements

Sound velocity measurements are performed through the analysis of the patterns detected by surface imaging and their evolution as a function of the delay time (i.e., producing a “movie”) [18]. In the liquid state, as in any elastically isotropic medium, phonon imaging patterns are circles, growing as a function of time, due to the arrivals of the spherical wave fronts generated by the focused pump beam at the opposite side of the sample (see the setup in Fig. 1).

An integrated profile is obtained from each image and then all the profiles are stacked as a function of time to produce a figure showing growing circles as a function of time (see Fig. 3). The theoretical expression of the radius as a function of time $R(t)$ is obtained by the following set of equations [18]:

$$\begin{aligned} z(t) &= v(t + mT_{\text{laser}} - \tau), \\ e_0 &= v(t_0 + mT_{\text{laser}} - \tau), \end{aligned} \quad (1)$$

$$R(t) = \sqrt{(z - e_0)\{[2C(z) - z] + e_0\}},$$

where $C(z) = z[1 + (\frac{z_R}{z})^2]$, v is the compressional sound velocity, $T_{\text{laser}} = 12.548(4)$ ns is the period between two subsequent pump laser shots, m is an integer which accounts for the number of shots between generation and detection, $\tau = 0.329$ ns is the pump-probe coincidence time that depends on the optical path difference between probe and pump beams, e_0 is the sample thickness, t_0 is the emergence time of the wave, and z_R is the acoustic Rayleigh length. A typical value of z_R is 15 μm but it depends on the quality of the pump beam focusing on the sample surface. In the case where the thickness of the sample e_0 is larger than z_R , Eq. (1) greatly simplifies as [26]

$$R(t) = v\sqrt{z(t)^2 - e_0^2}. \quad (2)$$

Parameters to be determined by the fitting process are then v , t_0 , and z_R . These are fixed or left free, depending on the features of each movie. The evolution of the radius of the second ($n = 2$) and third ($n = 3$) waves is not fitted, but calculated replacing e_0 by $(2n - 1)e_0$. With this method, the thickness e_0 and the sound velocity v are independently determined. The sound velocity data here obtained as a function of p and T are shown in Fig. 4 ([58], Sec. II A). Uncertainty on sound velocity is evaluated to be around 25 m/s.

Sound velocity data at ambient pressure as a function of temperature are numerous in the literature and are reviewed by Blairs [33] (compiling Refs. [34,61–66] and Fig. S3 in [58]).

On the contrary, sound velocity measurements as a function of pressure are scarce. Coppens *et al.* [34] performed

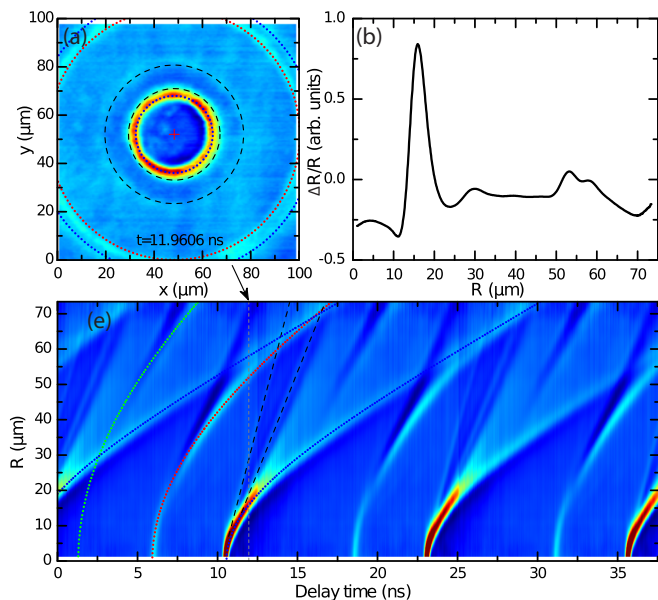


FIG. 3. (a) Phonon imaging pattern of the acoustic wave front at the liquid-diamond interface in liquid indium at 3 GPa and 682 K with collinear pump and probe at circular pattern center for 11.9606 ns pump-probe delay. (b) Integrated profile. (c) Integrated profiles stacked versus time. For clarity, the final image between 0 and T_{laser} is duplicated 3 times. The colored ripples and the lines show the radius of the circles detected at the sample surface versus time. The nonlinear $R(t)$ curves are linked to the volume waves propagating inside the sample and appearing at the surface, whereas the linear $R(t)$ curves are due to the pure surface waves (possibly surface skimming bulk waves propagating in the diamond at the interface diamond-sample [60]). Only the first nonlinear curve is fitted by the function $R(t)$, and the calculation with the obtained results is shown as the blue dotted line. The red and green dotted lines are calculations corresponding to multiple reflections in the sample ($n = 2$ and $n = 3$, respectively) and demonstrate the quality of the fit procedure.

pioneering measurements but only up to 1500 psi, i.e., around 0.01 GPa. More recently, Alatas *et al.* [35] and Komabayashi *et al.* [36] measured the sound velocities by inelastic x-ray scattering through the fit of the phonon dispersion curve $\omega(Q)$ [67]. Alatas *et al.* [35] measured sound velocity for only 3 data points up to 4.0 GPa and 633 K. Komabayashi *et al.* [36] extended the p - T range up to 923 K and 6.7 GPa. These data are however scattered, with large error bars, and for clarity are not shown in Fig. 4 where our data set is compared to the velocities obtained from the equation of state (EOS) [36].

The sound velocity is linked to the adiabatic bulk modulus B_S and the density ρ via the relation

$$v = \sqrt{B_S/\rho}; \quad (3)$$

then our measurements can be compared with values derived using the Komabayashi density-pressure-temperature relation [36] which requires only 6 thermoelastic parameters to calculate sound velocity: The density at ambient pressure ρ_0 , the isothermal bulk modulus $B_{T,0}$, the pressure derivative of the isothermal bulk modulus $B'_{T,0} = (\partial B_T/\partial p)_{p=0}$, the thermal expansion α_0 , the Anderson-Grüneisen parameter δ_T [68], and the Grüneisen parameter γ_G .

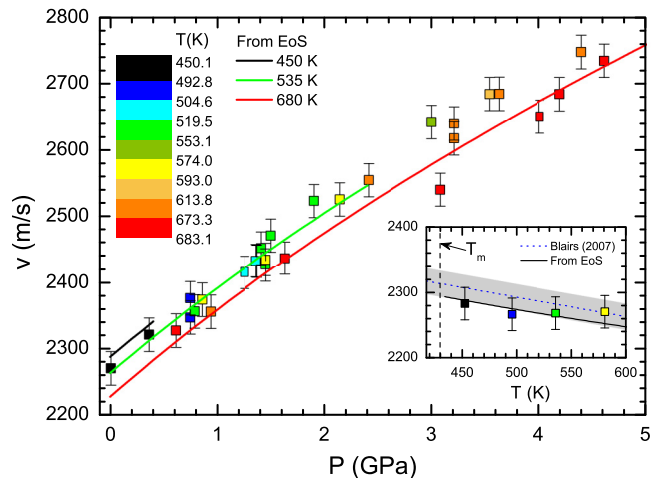


FIG. 4. Sound velocity in liquid indium as a function of pressure and temperature, measured by the phonon imaging method. The data are compared with velocities derived from the thermal EOS of Komabayashi *et al.* [36] calculated along three reference isotherms. Inset: Sound velocity as a function of temperature at ambient pressure, measured by the phonon imaging method [average thickness $e_0 = 68.3(12) \mu\text{m}$, with imposed parameter $z_R = 16.2(4) \mu\text{m}$] above melting temperature (T_M). The data are compared with the average linear relation of Blairs [33] (blue dotted line) and its dispersion (gray area; see Fig. S3 in [58]), and with the sound velocity calculated from the thermal EOS.

The density ρ is obtained from the isothermal Vinet EOS [69],

$$p = 3B_{T,0} \left(\frac{1-x}{x^2} \right) e^{\eta(1-x)} \text{ with } \eta = \frac{3}{2}(B'_{T,0} - 1), \quad (4)$$

where $x = (\rho/\rho_0)^{-1/3}$.

The thermal expansion α is calculated at any p and T using the Anderson-Grüneisen parameter δ_T ,

$$\alpha = \alpha_0 x^{3\delta_T}, \quad (5)$$

leading to the thermal EOS $\rho(p, T)$,

$$\rho = \rho_0 e^{-\alpha(T-T_M)}, \quad (6)$$

from which the bulk modulus is derived as

$$B_T = \rho \left(\frac{\partial p}{\partial \rho} \right)_T, \quad (7)$$

and finally the adiabatic bulk modulus is obtained as

$$B_S = B_T (1 + \alpha \gamma_G T). \quad (8)$$

Despite its simplicity, this model based on simpler assumptions than other thermal EOS formalisms (see, for example, Ref. [70]) well accounts for the thermodynamic quantities at ambient pressure when using parameters given in Ref. [36] from the seminal work of Kamioka *et al.* [46]: $\rho_0 = 7031.11 \text{ kg/m}^3$, $B_{T,0} = 32.8 \text{ GPa}$, $B'_{T,0} = 5.5$, $\alpha_0 = 12 \times 10^{-5} \text{ K}^{-1}$, $\delta_T = 5.5$, and $\gamma_G = 2.5$.

As shown in Fig. 4 this EOS, associated with previous inelastic x-ray scattering data [35,36], provide a good test of our experimental determination of the sound velocity at high pressure.

TABLE I. Thermodynamic data of liquid indium calculated from reference data $v(T)$, $\rho(T)$, $C_p(T)$, and the value of $(dv/dp)_{T,p=0}$ determined in this work.

T (K)	v (m/s)	ρ (kg/m ³)	C_p (J/kg K)	α_0 (10 ⁻⁵ K ⁻¹)	B_T GPa	dB_T/dT (MPa/K)	B'_T	δ_T	γ_G
T_M^0	2313.93	7022.00	258.0	10.85	34.02	-20.26	5.25	5.49	2.25
450	2307.90	7006.57	257.4	10.88	33.62	-20.01	5.25	5.47	2.25
500	2293.00	6968.47	256.0	10.93	32.63	-19.40	5.24	5.44	2.25
550	2278.10	6930.37	254.8	11.00	31.68	-18.81	5.23	5.40	2.24
600	2263.20	6892.27	253.8	11.06	30.75	-18.23	5.22	5.36	2.23
650	2248.30	6854.17	252.9	11.12	29.85	-17.66	5.21	5.32	2.22
700	2233.40	6816.07	252.2	11.18	28.98	-17.11	5.20	5.28	2.21
750	2218.50	6777.97	251.6	11.24	28.14	-16.58	5.19	5.24	2.20
800	2203.60	6739.87	251.2	11.31	27.33	-16.07	5.18	5.20	2.19
850	2188.70	6701.77	250.8	11.37	26.53	-15.59	5.16	5.17	2.17
900	2173.80	6663.67	250.4	11.44	25.77	-15.12	5.15	5.13	2.16
950	2158.90	6625.57	250.1	11.50	25.02	-14.68	5.14	5.10	2.14
1000	2144.00	6587.47	249.8	11.57	24.30	-14.26	5.13	5.07	2.13

Previous authors provided a data review and an accurate evaluation of thermodynamic quantities at ambient pressure: $v(T)$ [33], $\rho(T)$ [27], and $C_p(T)$ [71] (fitted by a third-order polynomial in Ref. [49]).

Following the seminal work of Shaw and Caldwell [72], these data, combined with the present accurate determination of $(dv/dP)_{T,p=0} = 121(6) \text{ m s}^{-1} \text{ GPa}^{-1}$, considered independently of the temperature, offer the opportunity to accurately calculate $B_{T,0}(T)$ and $B'_{T,0}(T)$ and to revise the equation of state up to ≈ 10 GPa. All the thermodynamic equations used are detailed in [58], Sec. II C. The calculated data are shown in Table I and are in very good agreement with Kamioka *et al.* [46], with the notable exception of α_0 and B_T , which must be revised by approximately -10% and $+4\%$, respectively ([58], Fig. S4).

Finally the equation of state of liquid indium is calculated from the thermodynamic parameters given in Table I and the isothermal Vinet EOS for each temperature. The results shown in Fig. 5 are close to Komabayashi *et al.* [36].

B. Determination of the melting curve

In this work, the melting of indium was determined using two different methods. The first method is the detection of the isothermal solid-liquid phase transition through a large difference in the delay time of the arrival of the first echo, a direct consequence of the changes in the sample thickness and mainly in the sound velocity upon transition [18] (see Fig. 6). The melting line was crossed along isotherms for increasing and decreasing pressures. This method is very accurate since the sound velocity is very sensitive to modifications in long-range order and consequently in the thermodynamic properties of the material. Noteworthy, the liquid-solid transition is always accompanied by a ‘‘plateau’’ in the curve of the sample pressure p as a function of membrane pressure p_m , likely a consequence of the volume variation at the transition ([58], Fig. S5).

The second method is the tracking of pressure and temperature for which liquid and solid phases coexist in equilibrium, and follow this along the melting line [75,76]. Here, we

remember that according to the Gibbs phase rule, for a single component system, T and p are not independent when two phases are in coexistence, as along the melting line (only one degree of freedom). The experimental protocol starts with measurements in the liquid, and then the temperature is continuously decreased (at a rate around 1 K/s). When the melting temperature is reached, the pressure in the sample chamber decreases due to volume reduction of the sample caused by partial solidification. Further volume reduction in both coexisting solid and liquid is expected due to the temperature decrease. These aspects favor the decrease in p concomitant to the imposed decrease in T along the melting line. However, due to the nontransparency of the sample, the visual observation of the solid-fluid equilibrium is impossible. The full transition of the sample into the solid is thus checked by three ways ([58], Fig. S7). First, the pressure stops to decrease although the temperature continues to decrease. Second, the transition from liquid to solid is observed by phonon

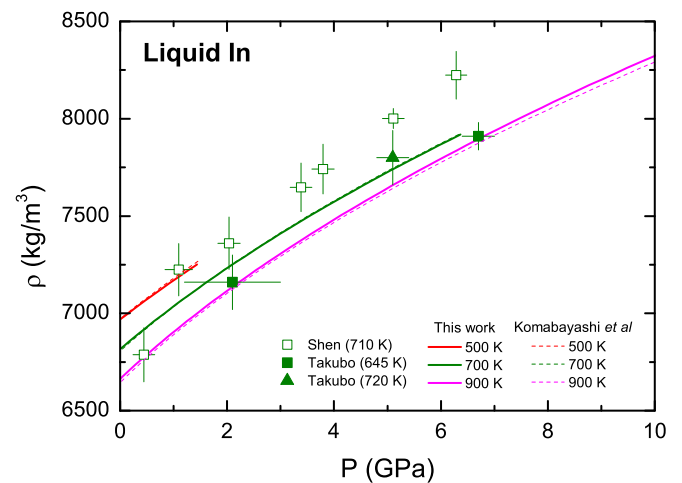


FIG. 5. Equation of state in liquid indium calculated from the Vinet EOS and thermodynamic parameters given in Table I (solid lines) compared to the EOS of Komabayashi *et al.* (dashed lines). The experimental data are from Shen [73] and Takubo [74].

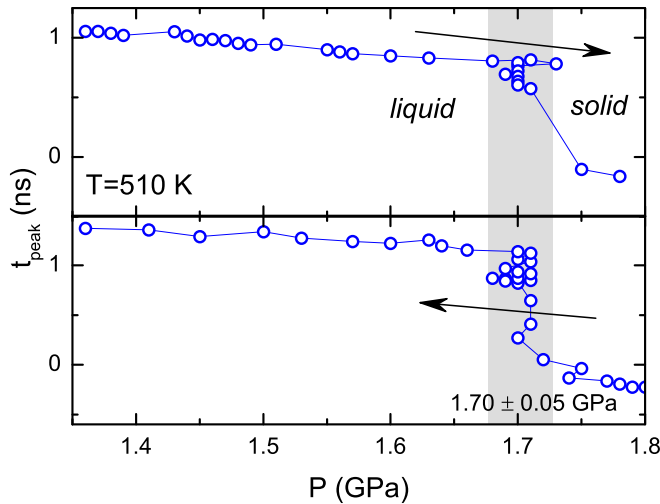


FIG. 6. Transition between liquid and solid indium (gray region) as recorded by the large and sharp variation of the arrival time of the first acoustic echo at $T = 510$ K. The transition pressure, measured both for increasing p (top panel) and decreasing p (bottom panel), is in this case $1.70(5)$ GPa.

imaging of the surface, with the apparition of noncircular patterns due to the elastic anisotropy of solid indium. Third, a large shift of the delay time of the echo peak is observed at the transition (similarly to what is shown in Fig. 6 as travel time modification upon phase transition is quite higher than the variations due only to the temperature or the pressure in the liquid phase; see also Fig. S7 in [58]).

The compilation of the measurements done by the two methods is presented in Fig. 7. The melting line is fitted by the widely used Simon-Glatzel equation [77],

$$T_M(p) = T_{\text{ref}} \left[\frac{p - p_{\text{ref}}}{a} + 1 \right]^{1/c}, \quad (9)$$

where $p_{\text{ref}} = 0$ GPa, $T_{\text{ref}} = T_M^0 = 429.74850(34)$ K are the well-known values used as secondary point of the international temperature scale (ITS) [30,31], and the two adjustable parameters a and c have been found to be $a = 4.61(11)$ GPa and $c = 1.792(34)$.

In order to check the consistency of our data, we can compare the slopes of the melting line at ambient pressure κ obtained by the Simon-Glatzel relation [see Eq. (10)] and by the Clausius-Clapeyron relation [see Eq. (11)].

From the Simon-Glatzel relation we obtain

$$\kappa = \left(\frac{dT_M}{dp} \right)_{p=0} = \frac{T_M^0}{ac} = 52.0(16) \text{ K/GPa}. \quad (10)$$

This value is higher than the values given by Jayaraman *et al.* (Table 3 in Ref. [79]) ranging from 43 to 50 K/GPa.

The Clausius-Clapeyron relation gives the slope of the melting line at ambient pressure as

$$\kappa_{\text{ref}} = \frac{T_M^0 (V_{m,\text{liq}} - V_{m,\text{sol}})}{\Delta H_{m,M}}, \quad (11)$$

where V_m are molar volumes in liquid and solid, and $\Delta H_{m,M}$ is the molar enthalpy of fusion (or melting). The quantities entering this relation measured at T_M and ambient pressure are

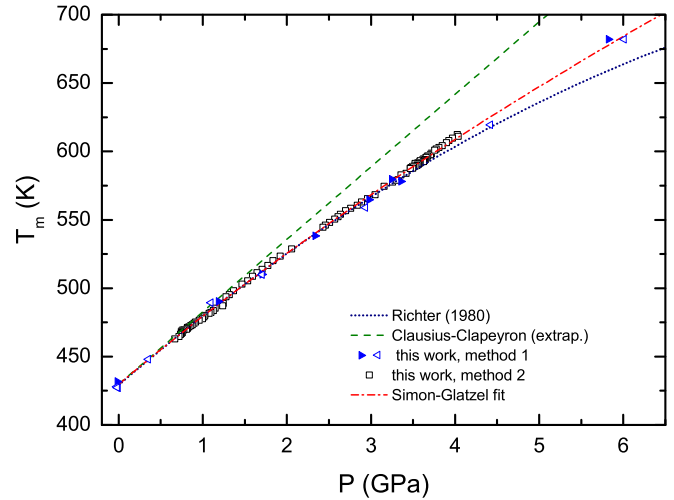


FIG. 7. Indium melting line measured by picosecond acoustics. As explained in the text, experimental (p, T) points are obtained in two ways. Method 1: Large and sharp shift of the arrival time of the first acoustic echo upon pressure increase (blue solid triangles) and upon pressure decrease (blue empty triangles) along isothermal paths; method 2: Through monitoring the liquid-solid equilibrium (empty black squares). All the data are fitted by a Simon-Glatzel equation [dash-dotted red line; see text and Eq. (9)]. In addition, an extrapolation of the Clausius-Clapeyron relationship at ambient pressure is shown [Eq. (11); green line], as well as the polynomial function given by Richter extrapolated above 3.5 GPa (black dotted line; see Table 1 in Ref. [78]).

carefully reviewed ([58], Sec. III B). Here we emphasize that the largest source of uncertainty in κ_{ref} comes from the value of ΔV_m , which is crucial to evaluate the consistency of the data [80]. The resulting $\kappa_{\text{ref}} = 53.1(48)$ K/GPa is in agreement with κ determined from the Simon-Glatzel relation.

To summarize, our determination of κ is in agreement with previous published values and gives further confidence in the reliability of our temperature measurements.

IV. DISCUSSION

The melting curve obtained in the present study and extrapolated up to 12 GPa, a pressure up to which no anomaly is expected in the liquid, is compared to the literature data in Fig. 8.

The disagreement between our data and the melting curve recently proposed by Errandonea [45] is evident for pressures above 3 GPa. In this work a Bridgman-type cell was employed up to 12 GPa and melting was identified as a drop in the resistance, measured with the 4-point technique, which is a well-proven melting criterion. Concerning metrology, the pressure scale used in their work relies on a calibration curve relating loading pressure and sample pressure, which is linear and well constrained by many reference points [86]. On the contrary, in the Bridgman pressure apparatus used, the temperature was measured by a thermocouple located 500 μm away from the center. Therefore temperature gradients could explain an underestimated temperature, to a larger extent than what is claimed by the authors (less than 25 K [45]). In further support of these remarks, the slope at ambient

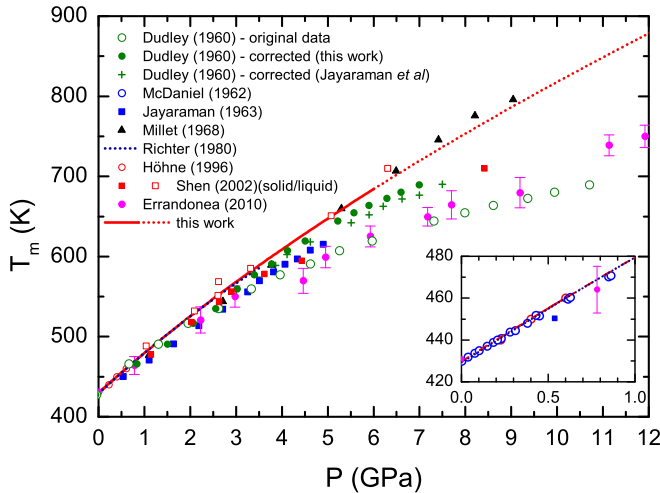


FIG. 8. The melting curve obtained in this work by picosecond acoustics (red line) and extrapolated above 6 GPa (red dotted line) is compared with the literature data: Dudley (1960) [32], Dudley corrected in this work, McDaniel (1962) [81], Jayaraman *et al.* (1963) [79] and their correction of the Dudley data, Millet (1968) [82] (data points are taken from Cannon (1974) [83]), Richter (1980) [78], Höhne (1996) [84], Shen (2002) [85] (red filled squares: Solid, red empty squares: Liquid), and Errandonea (2010) [45]. The inset shows the low-pressure region.

pressure of the melting curve determined by Errandonea is $\kappa = 45.2$ K/GPa, which is much lower than the expected reference value $\kappa_{\text{ref}} = 53.1(48)$ K/GPa and lower than our determination [$\kappa = 52.0(16)$ K/GPa].

Recently, Ma *et al.* [87] proposed an agreement with the measurements of Errandonea. However, this model is based on two experimental (p, T) data of the melting curve, which were directly taken from the measurements of Errandonea. Such a low melting temperature is also supported by the values of Dudley [32]. However, this work used an outdated pressure scale, subsequently proven to be inaccurate. Specifically, the Ba I-II transition pressure was assumed according to Bridgman [88], with $p_{\text{Ba I-II}} = 77.4$ katm = 7.843 GPa, while the revised value $p_{\text{Ba I-II}} = 5.50(5)$ GPa at 295.15 K was established in the subsequent work of Haygarth *et al.* [89]. In addition, Decker made a careful review (see Table 7 in Ref. [90] and related discussion) including the data of Haygarth and some other studies resulting in $p_{\text{Ba I-II}} = 5.53(12)$ GPa at 298.15 K. Based on this revised value, the calibration curve of Dudley can be corrected ([58], Sec. III C). The melting curve of Dudley before and after the correction is shown in Fig. 8. The so-corrected melting curve is in agreement with our data.

Richter [78] performed measurements in a piston cylinder up to 3.5 GPa and determined the melting curve by the differential thermal analysis (DTA) technique, carefully corrected for asymmetrical friction, and by the volumetric technique. The results obtained by the two techniques are consistent and yield a melting curve modeled according to a least-squares fit as $T_M = 156.0 + 52.6p - 2.25p^2$, where p is in GPa, and T_M is in degrees Celsius. Our data at low pressure are in excellent

agreement with these measurements, as well as with results of McDaniel *et al.* [81] and Höhne *et al.* [84].

Our data are extrapolated at pressures above 6 GPa according to Eq. (9). This extrapolation is in agreement with the melting temperatures of Shen measured by x-ray diffraction (XRD) [85], and in good agreement with Millet [82], despite the uncertainties of these measurements highlighted by Cannon [83].

V. CONCLUSION

In this work the phase diagram and the thermoelastic properties of liquid indium have been accurately investigated over an extended pressure and temperature range by picosecond acoustics measurements in combination with resistively heated diamond anvil cells. Particular care was devoted to the associated metrology. Indium was observed to be a very stable metallic compound at high pressure and high temperature, both in its solid and liquid phases. The thermodynamic properties of the liquid phase, well documented at ambient pressure as a function of temperature, have been here implemented to simultaneous high-pressure and high-temperature conditions, according to well-established thermodynamic formulations built on precise sound velocity measurements performed along selected isotherms. A p - ρ - T EOS for the liquid has been also derived.

The liquid-solid transition was determined through a clear and unambiguous criterium: The jump in time-of-flight measurements that directly relates to the changes of thermoelastic properties between the two phases. We have also constrained the melting curve by monitoring the liquid-solid equilibrium along several experimental runs. The results obtained by the two methods are consistent, and the measurements are in good agreement with the thermoelastic reference values of indium at ambient pressure.

Thanks to the careful metrology of pressure and temperature, our data offer an accurate determination of the melting curve, and the $T_M(p)$ line could be used as a calibration curve for future investigations.

Besides the specific interest of the case of indium, our study shows the reliability and versatility of the picosecond acoustic technique and associated methods, opening to the study of more complex or reactive liquid systems such as the alkali metals, sulfur, or phosphorus. Furthermore, since sound velocity is highly sensitive to the changes of the thermoelastic parameters, a similar approach can be used to probe first-order transitions other than melting, as well as more subtle transitions related to progressive changes in structure. Finally, studies can be extended over a larger pressure and temperature range using more performing resistive-heating systems rather than the simple external heater employed in this study. Experiments exploiting local or internal heaters for example can reach temperatures up to 1100–1300 K (e.g., [91,92]). Moreover, temperatures higher than 1000 K can be achieved by laser heating.

ACKNOWLEDGMENTS

This project has received funding from the European Research Council (ERC) under the European Union's Horizon

2020 research and innovation program (Grant Agreement No. 724690). Femtosecond laser micromachining at IMPMC has been developed and realized by the “Cellule Project” with

the financial support of ANR 2010-JCJC-604-01. The authors wish to thank Yoann Guarnelli for his help in DAC preparation.

- [1] H.-K. Mao, X.-J. Chen, Y. Ding, B. Li, and L. Wang, Solids, liquids, and gases under high pressure, *Rev. Mod. Phys.* **90**, 015007 (2018).
- [2] H. Tanaka, Liquid-liquid transition and polyamorphism, *J. Chem. Phys.* **153**, 130901 (2020).
- [3] F. D. Stacey, High pressure equations of state and planetary interiors, *Rep. Prog. Phys.* **68**, 341 (2005).
- [4] G. Morard, J. Bouchet, A. Rivoldini, D. Antonangeli, M. Roberge, E. Boulard, A. Denoeud, and M. Mezouar, Liquid properties in the Fe-FeS system under moderate pressure: Tool box to model small planetary cores, *Am. Mineral.* **103**, 1770 (2018).
- [5] H. Terasaki, A. Rivoldini, Y. Shimoyama, K. Nishida, S. Urakawa, M. Maki, F. Kurokawa, Y. Takubo, Y. Shibazaki, T. Sakamaki *et al.*, Pressure and composition effects on sound velocity and density of core-forming liquids: Implication to core compositions of terrestrial planets, *J. Geophys. Res.: Planets* **124**, 2272 (2019).
- [6] F. Xu, G. Morard, N. Guignot, A. Rivoldini, G. Manthilake, J. Chantel, L. Xie, A. Yoneda, A. King, E. Boulard *et al.*, Thermal expansion of liquid Fe-S alloy at high pressure, *Earth Planet. Sci. Lett.* **563**, 116884 (2021).
- [7] S. Anzellini and S. Boccato, A practical review of the laser-heated diamond anvil cell for university laboratories and synchrotron applications, *Crystals* **10**, 459 (2020).
- [8] P. Parisiades, A review of the melting curves of transition metals at high pressures using static compression techniques, *Crystals* **11**, 416 (2021).
- [9] Q. Williams, R. Jeanloz, J. Bass, B. Svendsen, and T. J. Ahrens, The melting curve of iron to 250 gigapascals: A constraint on the temperature at Earth’s center, *Science* **236**, 181 (1987).
- [10] R. Boehler, Temperatures in the Earth’s core from melting-point measurements of iron at high static pressures, *Nature (London)* **363**, 534 (1993).
- [11] O. T. Lord, E. T. Wann, S. A. Hunt, A. M. Walker, J. Santangeli, M. J. Walter, D. P. Dobson, I. G. Wood, L. Vočadlo, G. Morard *et al.*, The NiSi melting curve to 70 GPa, *Phys. Earth Planet. Inter.* **233**, 13 (2014).
- [12] R. Boehler, The phase diagram of iron to 430 kbar, *Geophys. Res. Lett.* **13**, 1153 (1986).
- [13] G. Morard, D. Andrault, N. Guignot, J. Siebert, G. Garbarino, and D. Antonangeli, Melting of Fe-Ni-Si and Fe-Ni-S alloys at megabar pressures: Implications for the core-mantle boundary temperature, *Phys. Chem. Miner.* **38**, 767 (2011).
- [14] S. Anzellini, A. Dewaele, M. Mezouar, P. Loubeyre, and G. Morard, Melting of iron at Earth’s inner core boundary based on fast x-ray diffraction, *Science* **340**, 464 (2013).
- [15] S. Boccato, R. Torchio, S. Anzellini, E. Boulard, F. Guyot, T. Irifune, M. Harmand, I. Kantor, F. Miozzi, P. Parisiades *et al.*, Melting properties by x-ray absorption spectroscopy: Common signatures in binary Fe-C, Fe-O, Fe-S, and Fe-Si systems, *Sci. Rep.* **10**, 11663 (2020).
- [16] J. M. Jackson, W. Sturhahn, M. Lerche, J. Zhao, T. S. Toellner, E. E. Alp, S. V. Sinogeikin, J. D. Bass, C. A. Murphy, and J. K. Wicks, Melting of compressed iron by monitoring atomic dynamics, *Earth Planet. Sci. Lett.* **362**, 143 (2013).
- [17] F. Decremps, M. Gauthier, S. Ayrinhac, L. Bove, L. Belliard, B. Perrin, M. Morand, G. L. Marchand, F. Bergame, and J. Philippe, Picosecond acoustics method for measuring the thermodynamical properties of solids and liquids at high pressure and high temperature, *Ultrasonics* **56**, 129 (2015).
- [18] S. Ayrinhac, M. Gauthier, G. L. Marchand, M. Morand, F. Bergame, and F. Decremps, Thermodynamic properties of liquid gallium from picosecond acoustic velocity measurements, *J. Phys.: Condens. Matter* **27**, 275103 (2015).
- [19] F. Decremps, S. Ayrinhac, M. Gauthier, D. Antonangeli, M. Morand, Y. Garino, and P. Parisiades, Sound velocity and equation of state in liquid cesium at high pressure and high temperature, *Phys. Rev. B* **98**, 184103 (2018).
- [20] S. Ayrinhac, V. N. Robinson, F. Decremps, M. Gauthier, D. Antonangeli, S. Scandolo, and M. Morand, High-pressure transformations in liquid rubidium, *Phys. Rev. Materials* **4**, 113611 (2020).
- [21] M. Kuriakose, S. Raetz, Q. M. Hu, S. M. Nikitin, N. Chigarev, V. Tournat, A. Bulou, A. Lomonosov, P. Djemia, V. E. Gusev, and A. Zerr, Longitudinal sound velocities, elastic anisotropy, and phase transition of high-pressure cubic H₂O ice to 82 GPa, *Phys. Rev. B* **96**, 134122 (2017).
- [22] S. Sandeep, T. Thréard, E. De Lima Savi, N. Chigarev, A. Bulou, V. Tournat, A. Zerr, V. E. Gusev, and S. Raetz, 3d characterization of individual grains of coexisting high-pressure H₂O ice phases by time-domain Brillouin scattering, *J. Appl. Phys.* **130**, 053104 (2021).
- [23] S. Raetz, M. Kuriakose, P. Djemia, S. M. Nikitin, N. Chigarev, V. Tournat, A. Bulou, A. Lomonosov, V. E. Gusev, and A. Zerr, Elastic anisotropy and single-crystal moduli of solid argon up to 64 GPa from time-domain Brillouin scattering, *Phys. Rev. B* **99**, 224102 (2019).
- [24] A. F. Goncharov, M. Gauthier, D. Antonangeli, S. Ayrinhac, F. Decremps, M. Morand, A. Grechnev, S. M. Tretyak, and Y. A. Freiman, Elasticity and Poisson’s ratio of hexagonal close-packed hydrogen at high pressures, *Phys. Rev. B* **95**, 214104 (2017).
- [25] F. Decremps, L. Belliard, B. Couzinet, S. Vincent, P. Munsch, G. Le Marchand, and B. Perrin, Liquid mercury sound velocity measurements under high pressure and high temperature by picosecond acoustics in a diamond anvils cell, *Rev. Sci. Instrum.* **80**, 073902 (2009).
- [26] S. Ayrinhac, M. Gauthier, L. E. Bove, M. Morand, G. Le Marchand, F. Bergame, J. Philippe, and F. Decremps, Equation of state of liquid mercury to 520 K and 7 GPa from acoustic velocity measurements, *J. Chem. Phys.* **140**, 244201 (2014).
- [27] M. J. Assael, I. J. Armyra, J. Brillo, S. V. Stankus, J. Wu, and W. A. Wakeham, Reference data for the density and viscosity of liquid cadmium, cobalt, gallium, indium, mercury, silicon,

- thallium, and zinc, *J. Phys. Chem. Ref. Data* **41**, 033101 (2012).
- [28] B. B. Alchagirov, R. K. Dadashev, F. F. Dyshekova, and D. Z. Elimkhanov, The surface tension of indium: Methods and results of investigations, *High Temp.* **52**, 920 (2014).
- [29] D. G. Archer and S. Rudtsch, Enthalpy of fusion of indium: A certified reference material for differential scanning calorimetry, *J. Chem. Eng. Data* **48**, 1157 (2003).
- [30] H. Abe, National standard and new reference material for specific heat capacity measurements, *Anal. Sci.* **37**, 201 (2021).
- [31] H. Preston-Thomas, The international temperature scale of 1990 (ITS-90), *Metrologia* **27**, 3 (1990).
- [32] J. D. Dudley and H. T. Hall, Experimental fusion curves of indium and tin to 105000 atmospheres, *Phys. Rev.* **118**, 1211 (1960).
- [33] S. Blairs, Review of data for velocity of sound in pure liquid metals and metalloids, *Int. Mater. Rev.* **52**, 321 (2007).
- [34] A. B. Coppens, R. T. Beyer, and J. Ballou, Parameter of nonlinearity in fluids. III. Values of sound velocity in liquid metals, *J. Acoust. Soc. Am.* **41**, 1443 (1967).
- [35] A. Alatas, H. Sinn, J. Zhao, A. H. Said, B. M. Leu, W. Sturhahn, E. E. Alp, G. Shen, and V. B. Prakapenka, Experimental aspects of inelastic x-ray scattering studies on liquids under extreme conditions (P-T), *High Press. Res.* **28**, 175 (2008).
- [36] T. Komabayashi, J. Kato, K. Hirose, S. Tsutsui, S. Imada, Y. Nakajima, and A. Q. Baron, Temperature dependence of the velocity-density relation for liquid metals under high pressure: Implications for the Earth's outer core, *Am. Mineral.* **100**, 2602 (2015).
- [37] K. Takemura, Effect of pressure on the lattice distortion of indium to 56 GPa, *Phys. Rev. B* **44**, 545 (1991).
- [38] O. Schulte and W. B. Holzapfel, Effect of pressure on atomic volume and crystal structure of indium to 67 GPa, *Phys. Rev. B* **48**, 767 (1993).
- [39] K. Takemura and H. Fujihisa, High-pressure structural phase transition in indium, *Phys. Rev. B* **47**, 8465 (1993).
- [40] A. S. Mikhaylushkin, U. Häussermann, B. Johansson, and S. I. Simak, Fluctuating Lattice Constants of Indium under High Pressure, *Phys. Rev. Lett.* **92**, 195501 (2004).
- [41] Y. Akahama, K. Takahashi, K. Kamiue, T. Sugimoto, N. Hirao, and Y. Ohishi, Pressure-induced reentrant structural transition and equation of state of indium, *J. Appl. Phys.* **125**, 075901 (2019).
- [42] G. V. Sin'ko and N. A. Smirnov, Structural transitions in indium under high pressure: *Ab initio* electronic structure calculations, *Phys. Rev. B* **74**, 134113 (2006).
- [43] G. Shen, N. Sata, M. L. Rivers, and S. R. Sutton, Melting of indium at high pressure determined by monochromatic x-ray diffraction in an externally-heated diamond anvil cell, *Appl. Phys. Lett.* **78**, 3208 (2001).
- [44] O. Degtyareva, Simple metals at high pressures, in *High-Pressure Crystallography*, NATO Science for Peace and Security Series B Physics and Biophysics, edited by E. Boldyreva, P. Dera (Springer, Dordrecht, 2010), pp. 261–280.
- [45] D. Errandonea, The melting curve of ten metals up to 12 GPa and 1600 K, *J. Appl. Phys.* **108**, 033517 (2010).
- [46] H. Kamioka, Change of ultrasonic wave velocity in indium near the melting point, *J. Phys. Soc. Jpn.* **52**, 2784 (1983).
- [47] L. Xu, Y. Bi, X. Li, Y. Wang, X. Cao, L. Cai, Z. Wang, and C. Meng, Phase diagram of tin determined by sound velocity measurements on multi-anvil apparatus up to 5 GPa and 800 K, *J. Appl. Phys.* **115**, 164903 (2014).
- [48] C. Su, Y. Liu, Z. Wang, W. Song, P. D. Asimow, H. Tang, and H. Xie, Equation of state of liquid bismuth and its melting curve from ultrasonic investigation at high pressure, *Phys. B: Condens. Matter* **524**, 154 (2017).
- [49] S. Ayrinhac, Heat capacity ratio in liquids at high pressure, *J. Appl. Phys.* **129**, 185903 (2021).
- [50] H. Maris, Picosecond ultrasonics, *Sci. Am.* **278**, 86 (1998).
- [51] O. Matsuda, M. C. Larciprete, R. L. Voti, and O. B. Wright, Fundamentals of picosecond laser ultrasonics, *Ultrasonics* **56**, 3 (2015).
- [52] Y. Sugawara, O. B. Wright, O. Matsuda, M. Takigahira, Y. Tanaka, S. Tamura, and V. E. Gusev, Watching Ripples on Crystals, *Phys. Rev. Lett.* **88**, 185504 (2002).
- [53] B. Perrin, B. Bonello, J. Jeannet, and E. Romatet, Interferometric detection of hypersound waves in modulated structures, *Prog. Nat. Sci.* **6**, S444 (1996).
- [54] S. Zhang, E. Peronne, L. Belliard, S. Vincent, and B. Perrin, Three-dimensional acoustic wavefront imaging in anisotropic systems by picosecond acoustics, *J. Appl. Phys.* **109**, 033507 (2011).
- [55] F. Datchi, A. Dewaele, P. Loubeyre, R. Letoullec, Y. Le Godec, and B. Canny, Optical pressure sensors for high-pressure–high-temperature studies in a diamond anvil cell, *High Press. Res.* **27**, 447 (2007).
- [56] J. Chervin, B. Canny, and M. Mancinelli, Ruby-spheres as pressure gauge for optically transparent high pressure cells, *Int. J. High Press. Res.* **21**, 305 (2001).
- [57] K. Syassen, Ruby under pressure, *High Press. Res.* **28**, 75 (2008).
- [58] See Supplemental Material at <http://link.aps.org/supplemental/10.1103/PhysRevMaterials.6.063403>, which contains Refs. [27,29–34,36,46,49,55–57,59,61–66,71,72,84,88–90,93–113], for additional details in the metrology (determination of p and T , Sec. I), the sound velocity measurements (including the thermodynamic relations used to deduce EOS for liquid indium, Sec. II), and the determination of the melting curve (including additional figures about “the second method” presented in the main text, and the determination of the slope of the melting curve from the Clausius-Clapeyron relation, Sec. III).
- [59] D. McCumber and M. Sturge, Linewidth and temperature shift of the R lines in ruby, *J. Appl. Phys.* **34**, 1682 (1963).
- [60] N. Chigarev, P. Zinin, D. Mounier, A. Bulou, L. Ming, T. Acosta, and V. Gusev, Analysis of ultrasonic echoes induced by pulsed laser action on an iron film in a diamond anvil cell, *High Press. Res.* **30**, 78 (2010).
- [61] O. Kleppa, Ultrasonic velocities of sound in some metallic liquids: Adiabatic and isothermal compressibilities of liquid metals at their melting points, *J. Chem. Phys.* **18**, 1331 (1950).
- [62] R. Turner, E. Crozier, and J. Cochran, A new technique for measuring the velocity of sound in liquid metals, *Can. J. Phys.* **50**, 2735 (1972).
- [63] P.-E. Berthou and R. Tougas, The compressibilities of liquid Sn-Tl, In-Bi, Sn-In, Bi-Sb, and Bi-Cd-Tl alloys, *Metall. Mater. Trans. B* **3**, 51 (1972).

- [64] D. Almond and S. Blairs, Ultrasonic speed, compressibility, and structure factor of liquid cadmium and indium, *J. Chem. Thermodyn.* **12**, 1105 (1980).
- [65] R. Bek, E. Nold, and S. Steeb, Röntgen-Beugungsuntersuchungen an Bi-In-schmelzen [in German; X-ray diffraction experiments with Bi-In-melts], *Z. Naturforsch. A* **36**, 150 (1981).
- [66] E. Pashuk and B. Pashaev, Temperature dependence of super-sound velocity and related volumetric dependence of the young modulus of some metals, *Teplofiz. Vys. Temp.* **21**, 479 (1983).
- [67] D. Antonangeli, F. Occelli, H. Requardt, J. Badro, G. Fiquet, and M. Krisch, Elastic anisotropy in textured hcp-iron to 112 GPa from sound wave propagation measurements, *Earth Planet. Sci. Lett.* **225**, 243 (2004).
- [68] F. Birch, Thermal expansion at high pressures, *J. Geophys. Res.* **73**, 817 (1968).
- [69] P. Vinet, J. Ferrante, J. R. Smith, and J. H. Rose, A universal equation of state for solids, *J. Phys. C* **19**, L467 (1986).
- [70] K. D. Litasov, P. I. Dorogokupets, E. Ohtani, Y. Fei, A. Shatskiy, I. S. Sharygin, P. N. Gavryushkin, S. V. Rashchenko, Y. V. Seryotkin, Y. Higo *et al.*, Thermal equation of state and thermodynamic properties of molybdenum at high pressures, *J. Appl. Phys.* **113**, 093507 (2013).
- [71] T. W. Chapman, The heat capacity of liquid metals, *Mater. Sci. Eng.* **1**, 65 (1966).
- [72] G. H. Shaw and D. A. Caldwell, Device for measuring sound speeds in reactive liquids at high pressure and temperature, *Rev. Sci. Instrum.* **56**, 1402 (1985).
- [73] G. Shen, N. Sata, M. Newville, M. L. Rivers, and S. R. Sutton, Molar volumes of molten indium at high pressures measured in a diamond anvil cell, *Appl. Phys. Lett.* **81**, 1411 (2002).
- [74] Y. Takubo, H. Terasaki, T. Kondo, S. Mitai, S. Kamada, T. Kikegawa, and A. Machida, Development of density measurement for metals at high pressures and high temperatures using x-ray absorption imaging combined with externally heated diamond anvil cell, *C. R. Geosci.* **351**, 182 (2019).
- [75] F. Datchi, P. Loubeyre, and R. LeToullec, Extended and accurate determination of the melting curves of argon, helium, ice (H₂O), and hydrogen (H₂), *Phys. Rev. B* **61**, 6535 (2000).
- [76] V. M. Giordano, F. Datchi, and A. Dewaele, Melting curve and fluid equation of state of carbon dioxide at high pressure and high temperature, *J. Chem. Phys.* **125**, 054504 (2006).
- [77] F. Simon and G. Glatzel, Remarks on fusion pressure curve, *Z. Anorg. Allg. Chem.* **178**, 309 (1929).
- [78] P. Richter and J. Clark, Asymmetrical friction in a piston-cylinder device and the effect on the melting curves of indium and bismuth, *Rev. Sci. Instrum.* **51**, 959 (1980).
- [79] A. Jayaraman Jr., W. Klement Jr., R. Newton, and G. Kennedy, Fusion curves and polymorphic transitions of the group III elements aluminum, gallium, indium, and thallium at high pressures, *J. Phys. Chem. Solids* **24**, 7 (1963).
- [80] E. Y. Kulyamina, V. Y. Zitserman, and L. Fokin, Titanium melting curve: Data consistency assessment, problems and achievements, *Tech. Phys.* **63**, 369 (2018).
- [81] M. L. McDaniel, S. E. Babb, and G. J. Scott, Melting curves of five metals under high pressure, *J. Chem. Phys.* **37**, 822 (1962).
- [82] L. E. Millet, Experimental melting curves of cadmium, indium, lead, tin, and zinc and Mössbauer measurements in iron to 90 kilobars, Ph.D. thesis, Brigham Young University, 1968.
- [83] J. F. Cannon, Behavior of the elements at high pressures, *J. Phys. Chem. Ref. Data* **3**, 781 (1974).
- [84] G. Höhne, W. Dollhopf, K. Blankenhorn, and P. Mayr, On the pressure dependence of the heat of fusion and melting temperature of indium, *Thermochim. Acta* **273**, 17 (1996).
- [85] G. Shen, N. Sata, N. Taberlet, M. Newville, M. L. Rivers, and S. R. Sutton, Melting studies of indium: Determination of the structure and density of melts at high pressures and high temperatures, *J. Phys.: Condens. Matter* **14**, 10533 (2002).
- [86] D. Errandonea, D. Martínez-García, A. Segura, J. Ruiz-Fuertes, R. Lacomba-Perales, V. Fages, A. Chevy, L. Roa, and V. Muñoz-San José, High-pressure electrical transport measurements on p-type GaSe and InSe, *High Press. Res.* **26**, 513 (2006).
- [87] J. Ma, W. Li, G. Yang, S. Zheng, Y. He, X. Zhang, X. Zhang, and X. Zhang, Modeling the pressure-dependent melting temperature of metals, *Phys. Earth Planet. Inter.* **309**, 106602 (2020).
- [88] P. W. Bridgman, The resistance of 72 elements, alloys and compounds to 100 000 kg/cm², *Proc. Am. Acad. Arts Sci.* **81**, 165 (1952).
- [89] J. Haygarth, I. Getting, and G. Kennedy, Determination of the pressure of the barium I-II transition with single-stage piston-cylinder apparatus, *J. Appl. Phys.* **38**, 4557 (1967).
- [90] D. L. Decker, W. Bassett, L. Merrill, H. Hall, and J. Barnett, High-pressure calibration: A critical review, *J. Phys. Chem. Ref. Data* **1**, 773 (1972).
- [91] D. Antonangeli, T. Komabayashi, F. Occelli, E. Borissenko, A. C. Walters, G. Fiquet, and Y. Fei, Simultaneous sound velocity and density measurements of hcp iron up to 93 GPa and 1100 K: An experimental test of the Birch's law at high temperature, *Earth Planet. Sci. Lett.* **331-332**, 210 (2012).
- [92] Z. Du, L. Miyagi, G. Amulele, and K. K. Lee, Efficient graphite ring heater suitable for diamond-anvil cells to 1300 K, *Rev. Sci. Instrum.* **84**, 024502 (2013).
- [93] G. J. Piermarini, S. Block, J. Barnett, and R. Forman, Calibration of the pressure dependence of the R₁ ruby fluorescence line to 195 kbar, *J. Appl. Phys.* **46**, 2774 (1975).
- [94] F. Datchi, R. Le Toullec, and P. Loubeyre, Improved calibration of the SrB₄O₇:Sm²⁺ optical pressure gauge: Advantages at very high pressures and high temperatures, *J. Appl. Phys.* **81**, 3333 (1997).
- [95] P. I. Dorogokupets and A. R. Oganov, Ruby, metals, and MgO as alternative pressure scales: A semiempirical description of shock-wave, ultrasonic, x-ray, and thermochemical data at high temperatures and pressures, *Phys. Rev. B* **75**, 024115 (2007).
- [96] These coefficients are different from those written in Ref. [55] because of a typo.
- [97] J. Hill and A. Ruoff, Temperature dependence of the velocity of sound in some liquid metals and eutectic alloys, *J. Chem. Phys.* **43**, 2150 (1965).
- [98] J. E. Hill and A. L. Ruoff, Velocity of sound measurements in liquid metals, *Rev. Sci. Instrum.* **36**, 1465 (1965).
- [99] M. Gitis and I. Mikhailov, Correlation of the velocity of sound and electrical conductivity in liquid metals, *Sov. Phys. Acoust.* **12**, 14 (1966).

- [100] H. J. McSkimin, P. Andreatch Jr., and R. Thurston, Elastic moduli of quartz versus hydrostatic pressure at 25 and -195.8°C , *J. Appl. Phys.* **36**, 1624 (1965).
- [101] E. Wilhelm, What you always wanted to know about heat capacities, but were afraid to ask, *J. Solution Chem.* **39**, 1777 (2010).
- [102] J.-P. Poirier, *Introduction to the Physics of the Earth's Interior* (Cambridge University Press, 2000).
- [103] T. B. Coplen, N. E. Holden, T. Ding, H. A. Meijer, J. Vogl, and X. Zhu, The table of standard atomic weights—an exercise in consensus, *Rapid Commun. Mass Spectrom.*, doi:10.1002/rcm.8864 (2020).
- [104] W. Roth, I. Meyer, and H. Zeumer, Atom-, schmelz- und umwandlungswärmen von gallium, indium und thallium, *Z. Anorg. Allg. Chem.* **214**, 309 (1933).
- [105] C. Gamertsfelder, Atomic distributions in liquid elements, *J. Chem. Phys.* **9**, 450 (1941).
- [106] P. Hidnert and M. G. Blair, Thermal expansivity and density of indium, *J. Res. Natl. Bur. Stand.* **30**, 427 (1943).
- [107] D. Williams and R. Miller, Densities of liquid and solid indium, *J. Am. Chem. Soc.* **72**, 3821 (1950).
- [108] A. Schneider and G. Heymer, Die temperaturabhängigkeit der molvolumina der phasen NaTl und LiCd, *Z. Anorg. Allg. Chem.* **286**, 118 (1956).
- [109] T. Iida, Y. Kita, Y. Kikuya, T. Kirihara, and Z.-i. Morita, Densities of Ga-In and In-Sn alloys in the solid and liquid states, *J. Non-Cryst. Solids* **117-118**, 567 (1990).
- [110] I. Getting, New determination of the bismuth I-II equilibrium pressure: A proposed modification to the practical pressure scale, *Metrologia* **35**, 119 (1998).
- [111] H. T. Hall and L. Merrill, Some high pressure studies on ytterbium, *Inorg. Chem.* **2**, 618 (1963).
- [112] M. Shimada, The effect of repeated loading on the generated pressure in a girdle high pressure apparatus, Contributions of the Geophysical Institute, Kyoto University **14**, 49 (1974).
- [113] M. Banus and S. D. Nye, Efficiency in a tetrahedral-anvil press as related to anvil and pyrophyllite size, *Rev. Sci. Instrum.* **35**, 1319 (1964).